ETH

Eidgenössische Technische Hochschule Zürich
Swiss Federal Institute of Technology Zurich

Characterization of Lumped-Element Superconducting Microwave Resonator Arrays for Analog Quantum Simulations

Semester Thesis

Kevin Küng

February 27, 2018

Supervisors: Dr. Anton Potočnik & Michele Collodo

Group leader: Prof. Dr. Andreas Wallraff

Quantum Device Lab, ETH Zürich

Abstract

We introduce laser scanning microscopy as a tool to characterize superconducting lumped-element microwave resonators and illustrate its application in mapping the normal-mode structure of microwave photons inside a 9-site linear array of resonators. The laser light locally perturbs resonator frequencies and induces shifts in resonance frequencies, which we determine by measuring the microwave transmission coefficient. From the magnitude of mode shifts, we can reconstruct spatial current distribution of the normal modes. Furthermore, we compare the data from laser scanning microscopy with a reconstruction of the system parameters from scattering coefficients.

Contents

Chapter 1

Introduction

Impressive experimental advances over the last two decades have turned the idea of quantum simulation [1] into reality [2, 3, 4, 5, 6, 7]. The competition between the different platforms isn't, however, a 'winner takes all' situation. Each platform has its own advantages and limitations, and different approaches often tackle complementary aspects of quantum simulation. What they have in common is their aim to solve problems that are computationally too demanding to be solved on classical computers, at least at the moment [8].

One suggested physical realization of photon-based quantum simulation consists of microwave photons inside large networks of superconducting resonators and qubits. This architecture is particularly promising because of the significant experimental progress in the field of circuit quantum electrodynamics (cQED) [9, 10, 11].

Previous work [12] [6] has shown the fundamental usefulness of laser scanning microscopy for quantum engineering. Despite the small lattices size, the exponential proliferation of Hilbert space dimension with increasing photon number quickly approaches the computational limits of a classical computer, rendering the system a quantum system in the rigorous sense. However, measuring and probing many-body states in such lattices still remains a significant experimental challenge [6].

In this work, we report measurements on a lumped-element superconducting microwave resonator arrays. Illuminating the resonator with optical photons, we observe a decrease in its resonance frequency and an increase in loss. We discuss characterization of normal-modes of a specific array's Hamiltonian. To compare results we have extracted design parameters from the scattering matrix elements.

Chapter 2

Modeling Coupled Lumped-Element Resonators

An electrical circuit can be thought of as a discrete network of lumped elements as long as the wavelength is large compared to the size of the circuit. The lumped-element model in this case is a simplified description of a spatially-distributed electrical system which can describe its behavior when certain conditions, as an inappreciable phase delay, are fulfilled. The model approximates the circuit by separating it into abstract discrete elements, leading to electrical quantities without their spatial component. In the case of a simple transmission line-based resonator this means that the main inductance and capacitance can be assigned to different parts distributed over the transmission line. These kinds of components offer practical advantages, such as their compact size and wider bandwidth characteristics [13].

In the realm of microwave circuits, we need to consider transmission line theory, as the design of microwave lumped-element circuits is based on small sections of TEM (Transversal Electromagnetic) lines. In contrast to circuit theory, where an electrical network is represented by idealized electrical components with the same current and voltage over their physical dimensions. In transmission line theory, we deal with a network of distributed parameters [14].

Inductor

An inductor is a passive electrical component which stores and releases magnetic energy. We characterize inductors with their respective inductance, which we can mathematically express as

$$v(t) = L\frac{di(t)}{dt},$$ (2.1)

where L is the inductance, $v(t)$ the voltage and $i(t)$ the current through the circuit.

Rubio Abdal [14] states that the inductance can be engineered by changing it per unit length if the transmission line by changing materials or geometry.

Capacitor

An ideal capacitor is an electric passive component which does not dissipate energy and which stores and releases electrical energy. The electrical energy is stored between two conductors separated by a dielectric. Capacitance is defined as

$$C = \frac{Q}{V}, \quad I = C\dot{V} \tag{2.2}$$

where Q is the charge stored and V the voltage.

2.1 Impedance of RLC Circuit

We can consider each element as an element with appropriate impedance

$$Z_C = \frac{1}{j\omega C}, \ Z_L = j\omega L, \ Z_R = R. \tag{2.3}$$

The total impedance in parallel or serial configuration is given by $Z^{-1} = Z_1^{-1} + Z_2^{-1}$ or respectively $Z = Z_1 + Z_2$.
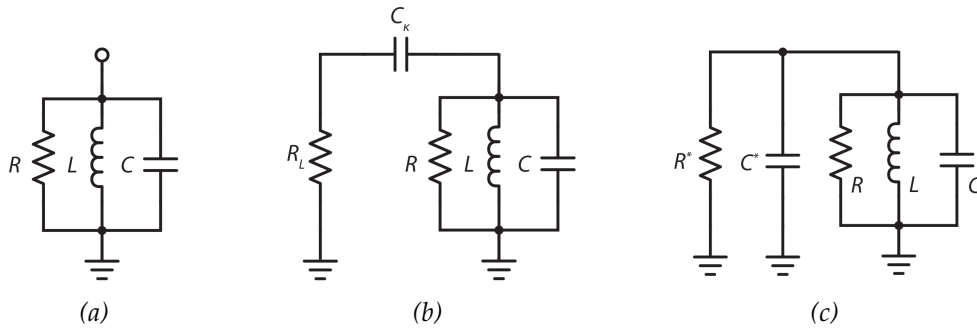

Figure 2.1: RLC Schematics. (a) Unloaded parallel RLC circuit. (b) Parallel RLC circuit with a capacitive coupling C_κ to the load R_L. (c) Norton equivalent of the capacitively coupled RLC oscillator.

For the unloaded RLC depicted in Fig. 2.1a, we have

$$\omega_0 \quad = \frac{1}{\sqrt{LC}}, \tag{2.4}$$

$$Z \quad = \sqrt{\frac{L}{C}}, \tag{2.5}$$

$$\gamma \quad = \frac{1}{RC} = \frac{\omega_0}{Q_{int}}. \tag{2.6}$$

The Q-factor is defined as

$$Q = \omega_0 \frac{\text{Energy Stored}}{\text{Power Loss}} = \frac{\omega_0}{\gamma} = \omega_0 RC = R/Z. \tag{2.7}$$

For a RLC resonator that is coupled to an external circuit (Fig. 2.1b) we use Norton's Theorem to transform to the Norton equivalent circuit (Fig. 2.1c) [13]:

$$C^* \quad = \frac{C_\kappa}{1 + (\omega_0 C_\kappa R_L)^2} \quad \approx C_\kappa \tag{2.8}$$

$$R^* \quad = \frac{1 + (\omega_0 C_\kappa R_L)^2}{\omega_0^2 C_\kappa^2 R_L} \quad \approx \frac{1}{C_\kappa^2 R_L \omega_0^2}, \tag{2.9}$$

such that the resonance frequency is $\omega_r = 1/\sqrt{LC_\Sigma}$, where $C_\Sigma = C + C^*$.

In the equivalent circuit, R^* describes external losses due to coupling to the load such as open transmission line. The external loss rate of the resonator to circuit is $\kappa = 1/(R^* C_\Sigma)$ and the internal loss rate is $\gamma = 1/(RC_\Sigma)$. This results in a loaded Q-factor of [14]

$$\frac{1}{Q_L} = \frac{1}{Q_{int}} + \frac{1}{Q_{ext}} = \frac{\gamma}{\omega_r} + \frac{\kappa}{\omega_r}. \tag{2.10}$$

2.2 Transfer Matrix Formalism

We can extend this approach to describe large linear system of coupled lumped- element resonators using ABCD (or transfer) matrix formalism. With

$$\begin{pmatrix} V_{\text{in}} \\ I_{\text{in}} \end{pmatrix} = \begin{pmatrix} A & B \\ C & D \end{pmatrix} \begin{pmatrix} V_{\text{out}} \\ I_{\text{out}} \end{pmatrix}, \tag{2.11}$$

we can represent the relation of voltage and current between the ports of a two-port microwave circuit.
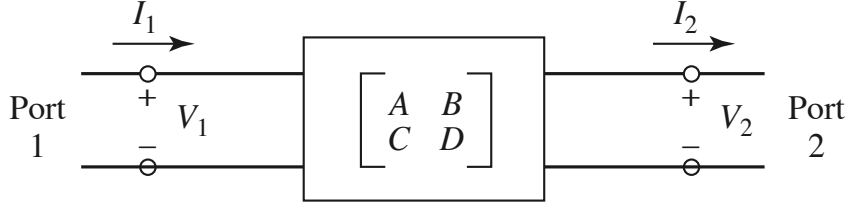
4

Figure 2.2: Two-Port Network [13]

To distinguish between parallel and serial components we write

$$M_S = \begin{pmatrix} 1 & Z \\ 0 & 1 \end{pmatrix}, \ M_P = \begin{pmatrix} 1 & 0 \\ Z^{-1} & 1 \end{pmatrix}. \tag{2.12}$$

The transfer matrix of one coupled RLC resonator is calculated by

$$M_{\mathrm{cRLC}} = M_S(C_\kappa) \cdot M_P(R) \cdot M_P(L) \cdot M_P(C), \tag{2.13}$$

which quickly gives rise to the generalization to several resonators coupled to a transmission line

$$M = \prod_{i=1}^{n} M_{\mathrm{cRLC},\, i} \quad \text{for } n \in \mathbb{N}. \tag{2.14}$$

The relation between impedance matrix of a two-port circuit to the transfer matrix is given by

$$\begin{pmatrix} Z_{11} & Z_{12} \\ Z_{21} & Z_{22} \end{pmatrix} = \begin{pmatrix} A/C & (AD - BC)/C \\ 1/C & D/C \end{pmatrix} \tag{2.15}$$

For impedance of a serial node:

$$A = \left. \frac{V_1}{V_2} \right|_{I_2=0} \tag{2.16}$$

which implies that $A = 1$. And similarly, for the other matrix components:

$$B = \left. \frac{V_1}{I_2} \right|_{V_2=0} = \frac{V_1}{V_1/Z} = Z, \tag{2.17}$$

$$C = \left.\frac{I_2}{V_2}\right|_{I_2=0} = 0, \tag{2.18}$$

$$D = \left.\frac{I_1}{I_2}\right|_{V_2=0} = 1. \tag{2.19}$$

Having the impedance of the system and knowing the characteristic impedance of a transmission line, this is the characteristic impedance of the waveguides used to couple to the resonator, typically 50 Ω - the reflection coefficient is

$$S_{11} = \left.\frac{V_1^-}{V_1^+}\right|_{V_2^+=0} = \left.\Gamma^{(1)}\right|_{V_2^+=0} = \frac{Z_{11} - Z_C}{Z_{11} + Z_C}. \tag{2.20}$$

We can find S_{21} by applying an incident wave at port 1, V_1^+, and measuring the outcoming wave at port 2, V_2^-. This is equivalent to the transmission coefficient from port 1 to port 2:

$$S_{21} = \left.\frac{V_2^-}{V_1^+}\right|_{V_2^+=0} \tag{2.21}$$

One could in principle write the reflection coefficient only in terms of the ABCD matrix

$$\Gamma = S_{11} = \frac{A + B/Z_C - CZ_0 - D}{A + B/Z_C + CZ_0 + D}. \tag{2.22}$$

with $B = 0$ and $D = 0$, since there are no currents flowing from the other side.

For a two-port transmission geometry we can apply the same approach leading to

$$S_{21} = \frac{2}{A + B/Z_C + CZ_C}. \tag{2.23}$$

2.3 Hamiltonian Description for Multiple Coupled Cavities

To start we will consider the Lagrangian of an electric circuit with N LC parallel oscillators coupled to each other capacitively, with the mode flux ($V_i = \dot{\phi}_i$) as a coordinate.

With Input-Output Theory we have the means to calculate, together with the Hamiltonian and intern/external loss rate, the scattering matrix of the underlying isolated system.

For an arbitrary number of Resonators N with square tridiagonal capacitance matrix $\mathbf{C}$ and diagonal inductance matrix $\mathbf{L}$ (inductance) we can write the Lagrangian as

$$\mathcal{L} = \underbrace{\frac{1}{2}\dot{\Phi}^{\mathsf{T}}\mathbf{C}\dot{\Phi}}_{\text{electric energy}} - \underbrace{\frac{1}{2}\Phi^{\mathsf{T}}\mathbf{L}^{-\mathbf{1}}\Phi}_{\text{magnetic energy}}, \quad \text{where } \Phi = (\phi_1, \dots, \phi_N). \qquad (2.24)$$

Using Legendre transform and the canonically conjugate momenta $Q_i \equiv \frac{\partial \mathcal{L}}{\partial \dot{\Phi}_i}$, we find the Hamiltonian of the System

$$\mathcal{H} = \frac{1}{2}Q^{\mathsf{T}}\mathbf{C}^{-1}Q + \frac{1}{2}\Phi^{\mathsf{T}}\mathbf{L}^{-\mathbf{1}}\Phi \qquad (2.25)$$

With the canonical commutator and by defining the second quantization's annihilation and creation operators, we find in rotating wave approximation

$$\mathcal{H} = \sum_i \hbar\omega_i(\hat{a}_i^\dagger \hat{a}_i + 1/2) + \sum_{i \neq j} \hbar J_{ij}(\hat{a}_i^\dagger \hat{a}_j + \hat{a}_j^\dagger \hat{a}_i) \qquad (2.26)$$

where

$$J_{ij} = \frac{1}{2}\frac{C_{ij}^{-1}}{\sqrt{C_{ii}^{-1}C_{jj}^{-1}}}\sqrt{\omega_i\omega_j} = \frac{1}{2}C_{ij}^{-1}\sqrt{Z_{ii}^{-1}Z_{jj}^{-1}}, \qquad (2.27)$$

and

$$\omega_i = \sqrt{\mathbf{C_{ii}^{-1}L_{ii}^{-1}}}. \qquad (2.28)$$

2.3.1 Eigenmodes and Eigenfrequencies

If we now choose some basis for $\mathcal{H}$, we can write the Hamiltonian as

$$\mathcal{H} = \hbar A^\dagger \underline{H} A \tag{2.29}$$

with $A = (\hat{a}_1, \hat{a}_2, \ldots, \hat{a}_N)$ a vector, $A^\dagger = \left(\hat{a}_1^\dagger, \hat{a}_2^\dagger, \ldots, \hat{a}_N^\dagger\right)$ a functional and

$$\underline{H} = \begin{bmatrix} \omega_1 & J_{12} & J_{13} & \cdots & & \cdots & J_{1N} \\ J_{12} & \omega_2 & J_{23} & & & & J_{2N} \\ \vdots & & & & & & \vdots \\ & & & \ddots & & & \\ & & & J_{i-1\,i} & \omega_i & J_{i+1\,i} & \\ \vdots & & & & & \ddots & \vdots \\ J_{1N} & \cdots & & & \cdots & J_{1-N\,N} & \omega_N \end{bmatrix}. \tag{2.30}$$

We then have as set of four nine-dimensional arrays parameters which completly define our model of the coupled resonator array (CRA). With **C**, L we can write the coupling matrix J_{ij} and the cavity modes ω_i. We note that the Hamiltonian of our circuit has nearest neighbor coupling $J_{i,i+1}$ as well as long range coupling $J_{i,i+k}$ for $1 < k \leq N - i$. However, for solving the eigenvalue problem of $\underline{H}$ the only numerically relevant terms are nearest neighbor coupling.

2.3.2 Input-Output Formalism

The Heisenberg equation with coupling rate (external loss) κ and internal loss γ can then be written as

$$\dot{a}_i = -\frac{i}{\hbar}[a_i, \mathcal{H}] - \frac{\kappa_i}{2}a_i - \frac{\gamma_i}{2}a_i + \sqrt{\kappa_i}a_{\mathrm{in},\,i}, \tag{2.31}$$

which are called Langevin equations.

$$S_{ij} = \sqrt{\kappa_i}\frac{a_i}{a_{\mathrm{in},\,j}} - \frac{a_{\mathrm{in},\,i}}{a_{\mathrm{out},\,i}} \tag{2.32}$$

Thus, together with the Input-Output relation [15]

$$\hat{a}_{in} + \hat{a}_{out} = \sqrt{\kappa}\hat{a} \tag{2.33}$$

the reflection coefficient for the single resonator is

$$S_{11} = \frac{a_{\text{out, 1}}}{a_{\text{in, 1}}} = \sqrt{\kappa}\frac{a}{a_{in}} - 1 = \frac{\kappa}{i(\omega - \omega_1) + (\kappa + \gamma)/2} - 1 \qquad (2.34)$$

and the transmission coefficient for the single resonator:

$$S_{12} = \frac{a_{\text{out, 1}}}{a_{\text{in, 2}}} = \frac{\kappa}{i(\omega - \omega_1) + (\kappa + \gamma)/2} \qquad (2.35)$$

For an arbitrary number of resonators, we will have a system of N coupled ordinary differential equations.

Chapter 3

Theory of Photo Response and Laser Scanning Microscopy

Laser scanning microscopy makes it possible to gather local information about photon occupancies in such lattices. For instance, it allows us to locally image normal modes in a microwave resonator array. When illuminating a superconducting structure with a laser the cooper pairs break into quasiparticles. In this experiment a Laser with 405 nm at 1 V which results in 10 mW at the structure. This increases kinetic inductance and ohmic losses R of the circuit [6].

In superconductors there exist two types of charge carriers:

- Cooper pairs. Free electrons binding together by photon-electron interaction. They can condense in a superconducting state where current can flow dissipationless below the critical temperature T_C,

- Quasiparticles. Free charge particles with renormalized mass. They dissipate energy due to scattering with phonons.

Microwave power $P_{\text{rf, ab}}$ is absorbed by the quasiparticles, which can exchange energy with a bath of phonons with distribution $n(\Omega)$. The phonons are also connected to a thermal bath and an effective hot phonon source that accounts for optical absorption. The absorbed optical power P_{opt} acts as an additional phonon generating source term. The Fig. 3.1 shows the thermal model of our system [7].

The total inductance of a superconducting circuit is then given by

$$L = L_{kin} + L_m, \tag{3.1}$$

where L_{kin} is the kinetic inductance and L_m the geometric inductance. With this model we derive using Kirchhoff's laws the photo response of the system with one resonator. The voltage equation is
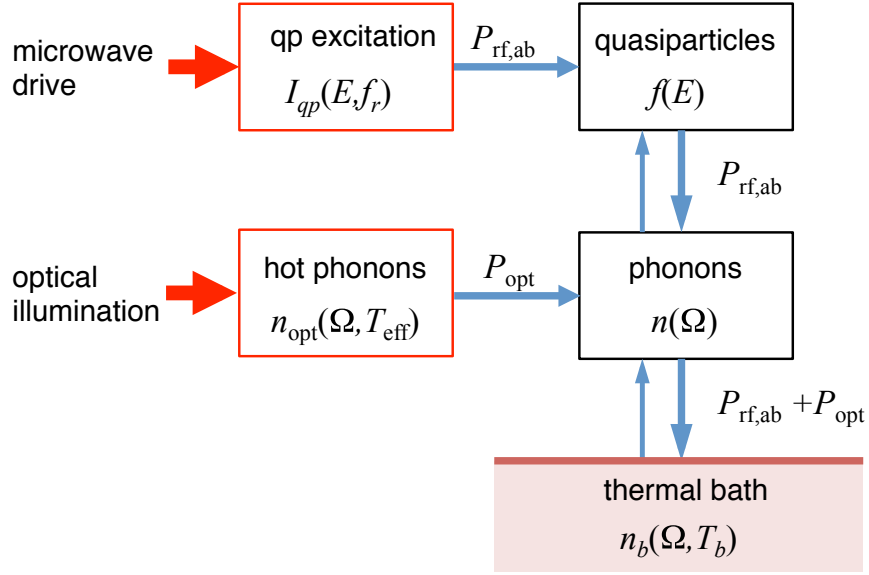
Figure 3.1: Diagram showing model for steady-state power flow in the quasiparticles and phonons in a thin-film superconducting resonator under optical illumination [7]

.

$$V_C + V_{L_m} + V_{L_{kin}} + V_R = 0. \tag{3.2}$$

By substituting $V_C = Q/C$, $V_{L_m} = L_m\dot{I}$, $V_{L_{kin}} = L_{kin}\dot{I}$, and $V_{R^*} = R^*I$, we have

$$\frac{Q}{C} + L_m\dot{I} + L_{kin}\dot{I} + RI = 0. \tag{3.3}$$

Taking time derivative, we can write equation of motion as

$$\ddot{I} + \frac{R}{L_m + L_{kin}}\dot{I} + \frac{1}{(L_m + L_{kin})C}I = \ddot{I} + \gamma\dot{I} + \omega_0^2 I = 0. \tag{3.4}$$

Comparing coefficients, we get the internal loss term

$$\gamma = \frac{R}{L_m + K_{kin}} \tag{3.5}$$

and the resonant frequency

$$\nu_0 = \frac{\omega_0}{2\pi} = \frac{1}{2\pi\sqrt{LC}} \tag{3.6}$$
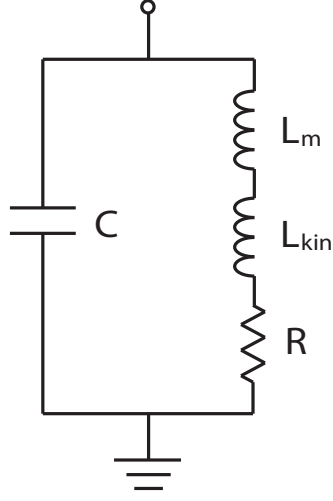
11

Figure 3.2: The circuit model of an unloaded parallel superconducting lumped element resonator. In the figure, C is capacitance, L_M is geometric inductance, L_{kin} is kinetic inductance, and R is effective resistance given by two-fluid model [12].

Under small laser perturbation, ΔL_{kin} and ΔR^* are directly proportional to laser power but independent of microwave power [16]:

$$\Delta \nu_0 = -\frac{1}{4\pi\sqrt{C}}\frac{\Delta L_{kin}}{(L_m + L_k)^{3/2}}, \tag{3.7}$$

$$\Delta \gamma = \frac{\Delta R}{L_m + L_{kin}}. \tag{3.8}$$

As Culbertson et al. [17] have pointed out, to measure a photo response the laser must shine on the inductor (where current density J is high). We have

$$\delta \nu_0, \ \delta \gamma \propto J^2, \ P_L \tag{3.9}$$

where P_L is the laser power and current density J.

The approach used in this thesis for defining photo response is to measure the distance in the IQ-Plane for ω_0 an eigenfrequency and the points Γ_{on}, $\Gamma_{\text{off}} \in \mathbb{C}$,

$$|\Gamma_{\text{on}}(\omega_0) - \Gamma_{\text{off}}(\omega_0)| = \frac{1}{2}\left|\kappa\left(\frac{1}{\gamma + \kappa} - \frac{4}{\gamma + \delta\gamma - 2i\delta\omega_0 + \kappa}\right)\right| \tag{3.10}$$
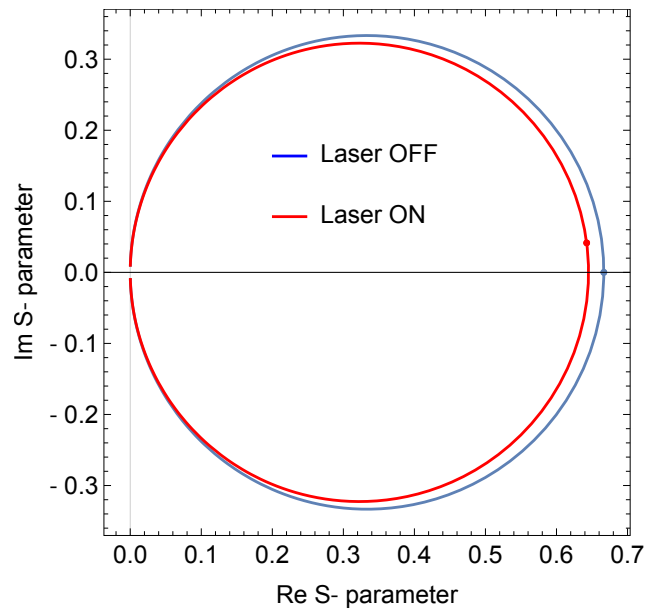
Figure 3.3: An theoretical illustration of photo response in the IQ-Plane with values close to our experimental setup. The graph in red is —$\Gamma_{on}(\omega)$|*, the graph in blue* —$\Gamma_{off}(\omega)$|*.*

Chapter 4

Experimental Details

The Quantum Device Lab uses superconducting planar waveguides for microwaves as a framework for analog quantum simulations with photons. The use of lumped-element resonators in circuit QED architecture is less common due to unwanted stray fields and parasitic element values which complicate the design procedure. To solve the design problem, an iteration using finite- element numerical simulations and fabricated device measurements is usually employed in order to reach the desired properties. Although such method has proven to be useful for smaller structures, it becomes computationally much harder in case of large number of elements, something that is desired in complex classical and quantum circuits. Here we observe structures of nine lumped-element resonators.

The arctic cryostat (see Fig. 4.2), laser scanning microscope and microwave spectroscopy setup used in this thesis was developed by G. Puebla-Hellmann in his PhD thesis [18] and improved in later work [12] [19] [16].

A cryostat based on a pulse-tube cooler, using the exibility of a custom system to implement a low-vibration setup referenced to an optical table was used as the main setup. The name is inspired by its intended use: trAnsport, Rf and optiCal Three kelvIn Cryostat (Arctic), although it is not a true acronym [18].

Furthermore, the setup should feature fast cycle times and simple operation to allow a high sample throughput. To further increase the throughput of the Arctic setup we used a helium Dewar and a dipstick - a rigid assembly housing the microwave cables and supporting the sample depicted in Fig. 4.1. This allows for quick measurement with a Agilent N5230 vector network analyzer and characterization of samples. Samples with the best design characteristics will get analyzed further with scanning defect microscopy.

Figure 4.1: Sample holder which is attached to the end of the dipstick. The chip is placed on the copper PCB (third component from the right) and fully enclosed in the copper shielding. This shielding is then fully submerged into liquid helium [20].
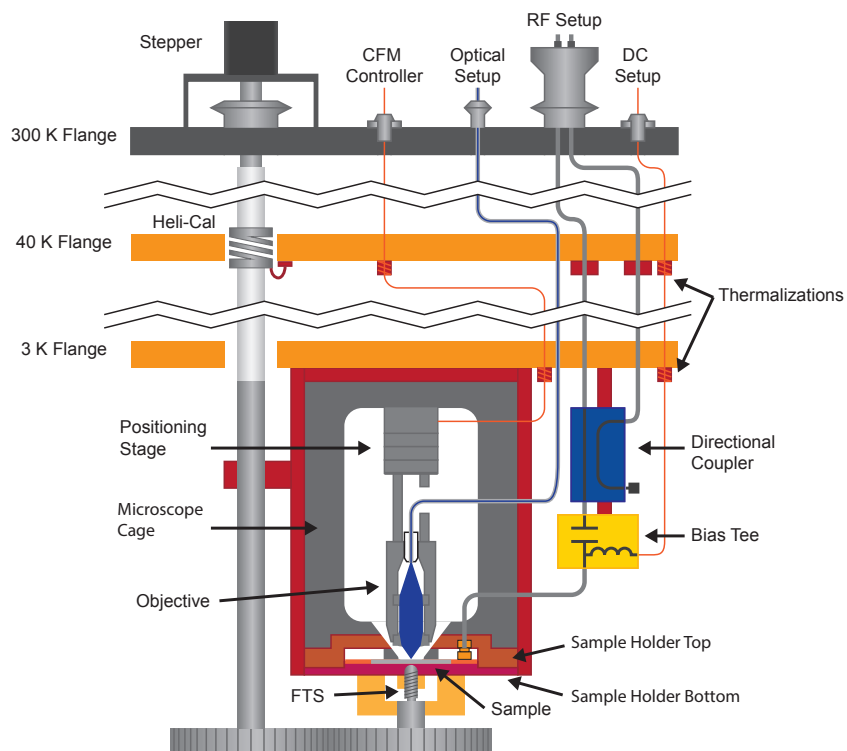

Figure 4.2: Schematic of the general experimental setup in the Arctic cryostat [18]

4.1 Design of Coupled Microwave Resonator Arrays

The planar lumped element resonators were fabricated using a standard photolithography procedure with a 1.6 μm thick AZ5241E photoresist. Devices are structured on a 450 μm thick sapphire substrate sputtered with 150 nm thick Nb layer. Coming from the design paradigm of Mask 66, characterized with details in Tab. 4.1 and shown in Fig. 4.3a, 4.3b, the new features to experimentally test is a top-bottom (TB) symmetry, dummy resonators (D) on the edge shown in Fig. 4.3.

	Meander Inductor (L)
No. of turns	21
Turn length (h)	220 μm
Line width (w)	3 μm
Gap width (d)	3 μm

Table 4.1: Design details of the meandering inductors on the M92 chip series. Note that the inductors in our design are in parallel, hence the total inductance of one site is half of the inductance for a single inductor $L \approx 0.74$ nH.

	C	C_κ	C_t
Finger no.	36 (4 x 9)	5	9 / 10 / 11
Finger length	197 μm	98 μm	98 μm
Finger width	3 μm	2 μm	2 μm
Finger gap	3 μm	2 μm	2 μm

Table 4.2: Design details of the interdigital capacitors used for the M92 chip [14].

(a) M92 BR9: Bottom-Reflection-9 resonator array

(b) M92 BT9: Bottom-Transmission-9 resonator array

(c) M92 TBT9: Top-Bottom-Transmission-9 resonator array

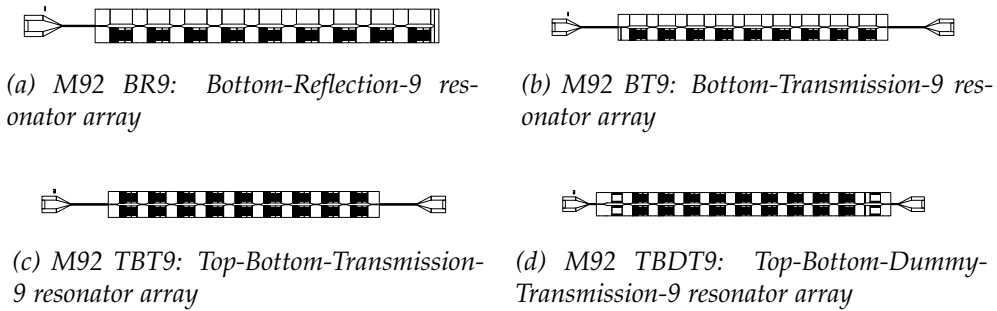*(d) M92 TBDT9: Top-Bottom-Dummy-Transmission-9 resonator array*

Figure 4.3: CAD-Design examples of major design paradigms of samples on Mask92

For measuring reflection and transmission of microwave photons through

16

the structure the coupled resonator array is coupled to the high temperature electronics and launchers with a coupling of capacitances C_κ. Between every individual resonator in the array we have a finger capacitator with coupling capacitances C_J [21].
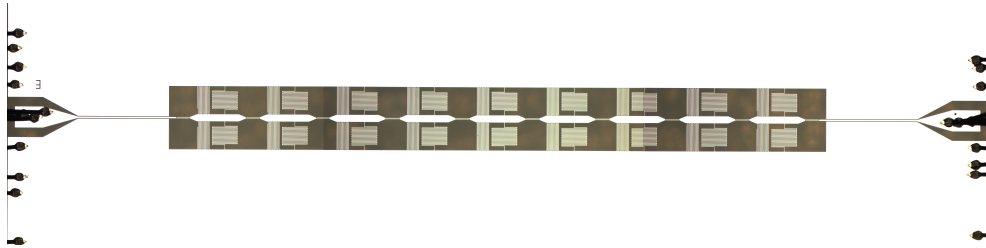

Figure 4.4: The TBT9-array on the current mask M92. Specific features are the top-bottom symmetry and two-finger coupling capacitators. Please notice that this is an array without dummy resonator at the edge. The coupling capacitor has a lenght of around 100 μm.

Geometrically, all resonators are nominally identical and equipped with two features, inductors and capacitors. Meander inductors are a space efficient way of reaching high capacitance. Interdigitated (finger) capacitors offer the simplicity of an integrated capacitor without the need of a multilayer fabrication process and with moderate capacitance values [14].

In Fig. 4.5 a false micrograph of the previous iteration Mask 66 is shown. This design featured only one axis of symmetry. The new iteration Mask 92 as shown in the App. Fig.A introduces a top-bottom symmetry of the meander inductors and shunt capacitors, which should lead to reduced edge effects from edge currents that have to flow around the structure (see Fig. 4.3b).

To reduce edge effects that result from microwave currents flowing from the resonators at the edge to the ground, the design choice was to incorporate dummy resonators to have emptier neutral space between the edge resonators and ground in one direction. A dummy resonator is an island with no meander inductor or shunt capacitor as shown in Fig. 4.6 and 4.7.
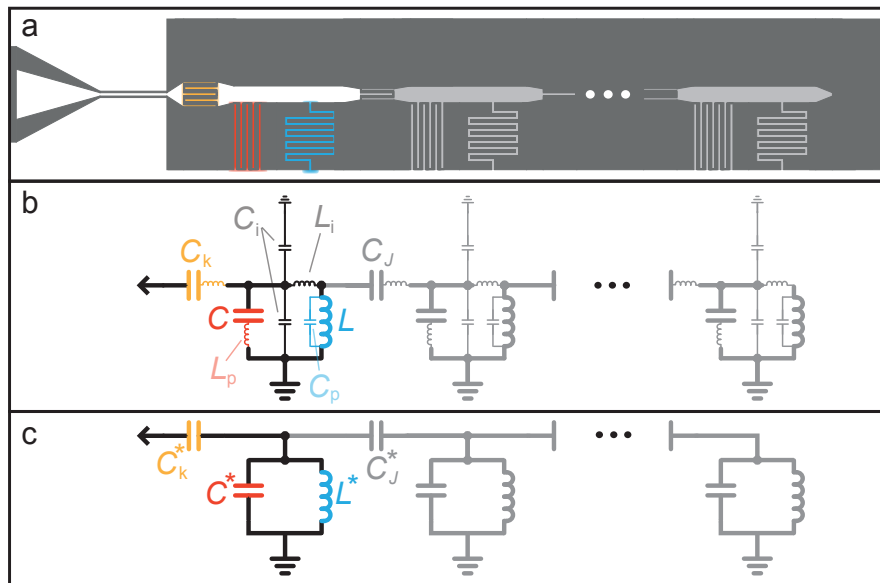
Figure 4.5: (a) False micrograph of designed lumped element coupled LC oscillator array. Sapphire substrate is depicted in dark gray, all other structures are thin Nb layer on top of the substrate. The structure on the left is the input and output transmission line. In the first oscillator the interdigitated coupling capacitor (orange), interdigitated shunt capacitor (red) and meander inductor (blue) are indicated. (b) Lumped-element model with parasitic elements. (c) Effective lumped-element model where element values are renormalized to compensate for parasitic contributions (Courtesy of Anton Potočnik).
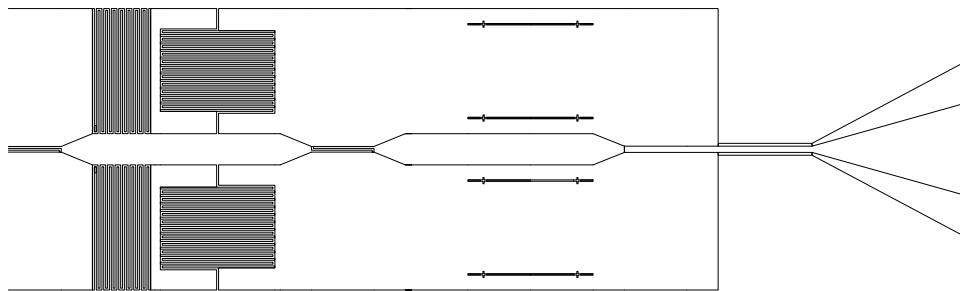

Figure 4.6: A CAD blueprint of a dummy resonator between top-bottom symmetric resonator and a launcher to the right.
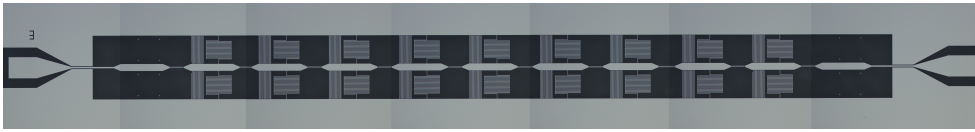
Figure 4.7: The TBDT9-array on the current mask M92. Specific features are the top-bottom symmetry and two-finger coupling capacitators and dummy resonator on the edges. The coupling capacitor has a length of around 100 μm.

4.2   Optical Setup

The setup consists of three parts, one part generating and regulating the excitation laser, another distributing the laser into the fiber and detecting reflection and possible emission and finally the low-temperature part, consisting of the moving stage and the objective, all of which will be discussed in the following [18].

The Fig. 4.8 shows a schematic overview of the optical setup. At the fiber output, the light is split into two beams, one entering the fiber of the CFM (confocal microscope), the second being used to determine the intensity of the arriving light via a photo-detector. The intensity signal is then fed into a PID controller connected to the AOM driver, creating a feedback loop.

An acousto-optic modulator (AOM) is used to control the laser intensity, allowing the laser diodes to run at a constant current and leading to a stable output spectrum, as the diodes are not frequency locked and the laser frequency and width depend on the current. The AOM is based on the acousto-optic effect, a scattering process between phonons and photons in an optical crystal.

An Attocube piezoelectric positioning system allows for adjusting position of the lense. It scans through x and y direction for changing position of the laser over specific feature of the sample, whereas z-direction positioning allows to focus the beam. The ASC500 and ANC350 are used to perform 2D scan over the sample and are controlled with a software suite called Daisy. We have to modes: The Scanner is designed for maximum range of 30 μm $\times$ μm at cryogenic temperatures. It can resolve individual features of the sample like single conductor lines. The Stepper mode achieves large scale scans of 4 mm $\times$ 4mm.
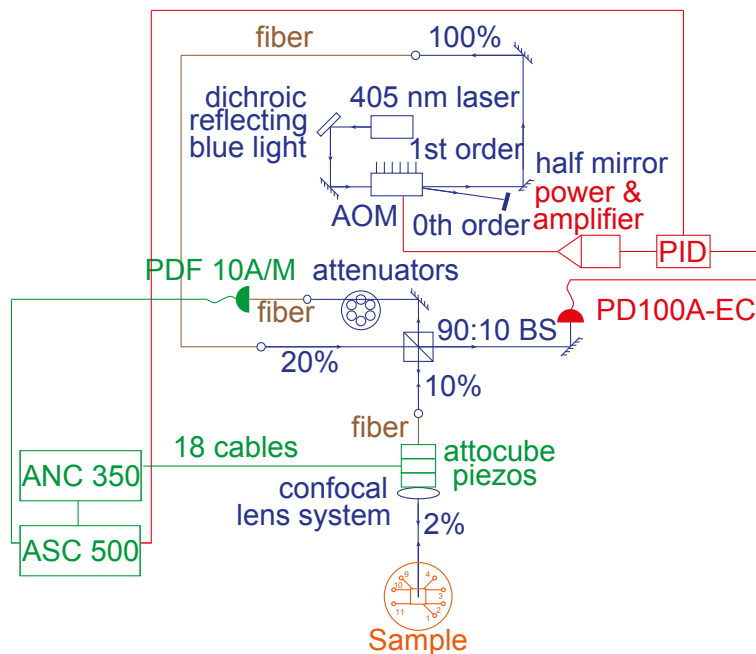
Figure 4.8: The optical setup used in the experiments. Based on [22].

4.3 Microwave Setup

The Microwave signal is generated by two SMB100A low noise RF microwave signal generators. One of them is directly connected to the sample in the fridge. The other is connected to the LO port of an IQ mixer acting as LO signal. The RF frequency and the LO frequency differ by Δf. After the conversion with the IQ mixer, IQ quadratures have frequency Δf and are measured by either the ASC500 or a FPGA (field-programmable gate array). This second arm provides a phase reference to preserve the phase relation between the local oscillator (LO) and the RF input. It is not preserved during a frequency change at the signal generators. The signal from the RF generator is fed through a -20 dB attenuator, before being amplified in a down conversion arm similar to the one amplifying the reflection signal from the fridge. The signal is fed into input B at the FPGA. The red box denotes the down-conversion arm that exists twice where the red symbols are the alternative connections for the second arm. A constant phase relation is achieved by multiplying input A with complex conjugated input B.
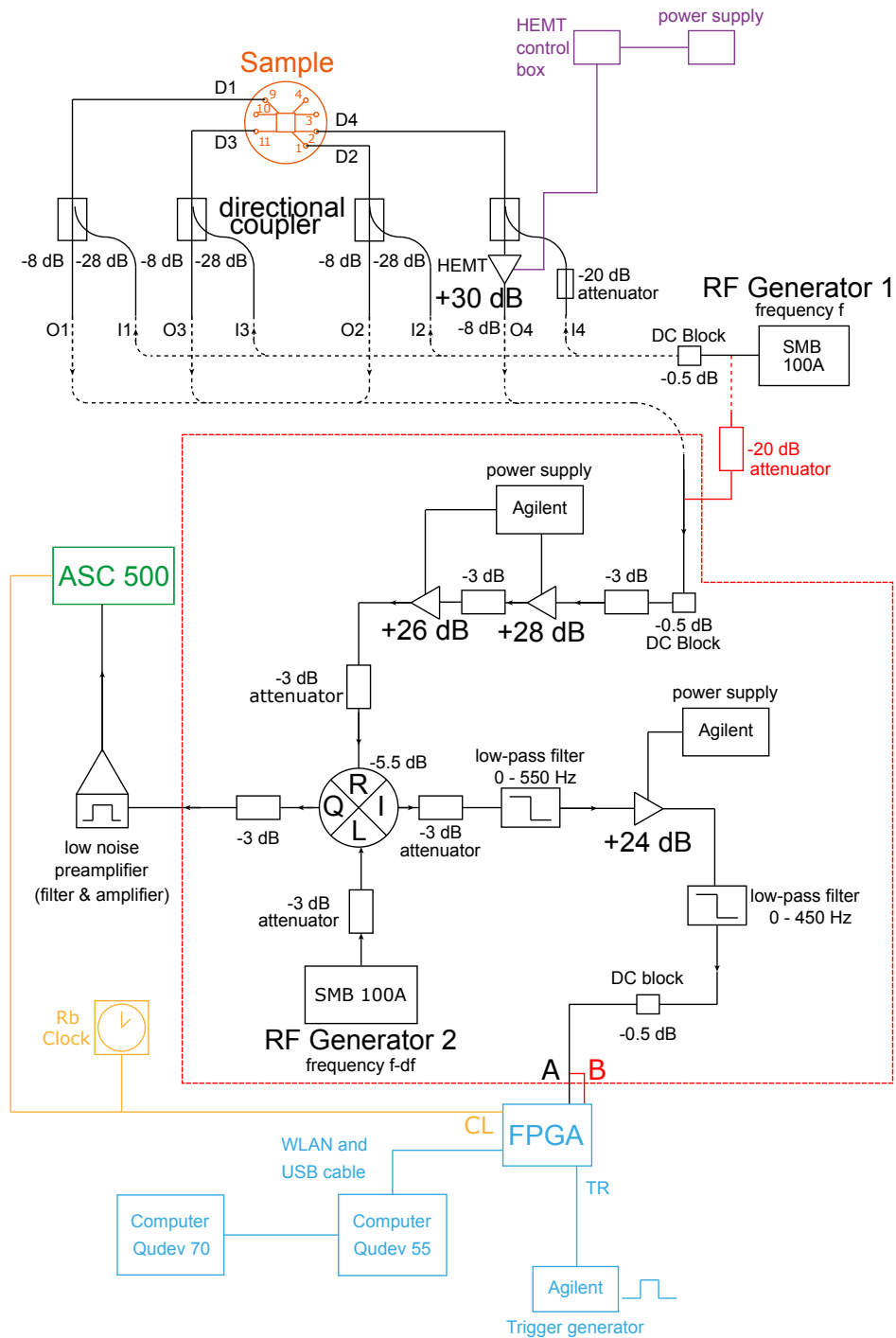
Figure 4.9: The microwave setup used in the experiments. The red dashed box exists twice. The second time as a reference arm, where it is connected with the red lines. Based on [22].

4.4 Signal Processing and Measurement of Photo Response

There are two ways to measure Photo response with our setup. Subtracting $|\Gamma_{\text{on}} - \Gamma_{\text{off}}|$ and calculating $|PR| = \sqrt{|PR_I|^2 + |PR_Q|^2}$ requires two measurements to get meaningful photo response result. By using DiffMode in FPGA, it is possible to perform the task in one measurement.

Voltage photo response is data proportional to ADV voltage at the FPGA. Similarly, to measure a power photo response signal, it is required that the AWG triggers the FGPA while being synchronized to laser intensity modulation and measuring microwave power at the FGPA.

The Fig. 4.10 shows a screen shot in Cleansweep and schematic in FPGA of the signal math control tap. In the tap, one can choose the definition of signal a and b, the product of which is the output of the signal math section, which are named s_A and s_B for signal from different ADCs. The decimator following signal math processing allows one to discard some of the data in a series of repeating measurement. The Correlator and Averager do the final signal processing before it is written in to RAM.
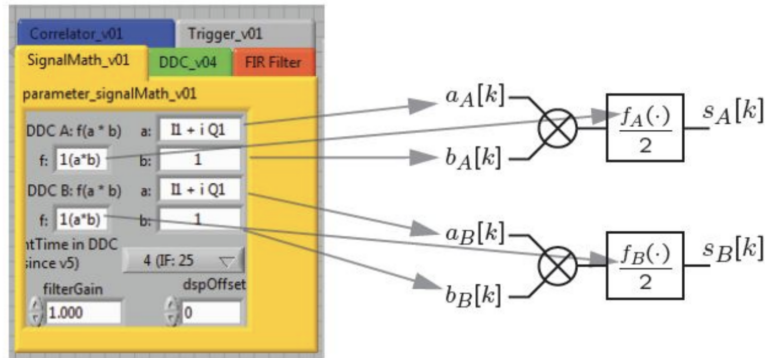

Figure 4.10: Schematic of SignalMath v01 in Cleansweep, which controls how FPGA proceeds I and Q quadratures from digital down-conversion. DDC is an abbreviation of digital down-conversion [12].

The Fig. 4.11 shows the schematics of Correlator and Averager. In the Correlator, the two signals from signal math section are first Fast Fourier transformed, and then s_B is converted to its complex conjugate. The two signals are then multiplied at a multiplier. The Averager sums up the result of N repeating measurements, where N is specified by averageLengthExp option under the Correlator tap in Cleansweep. One can choose to turn on and off some functions of the Correlator and Averager on the control panel in

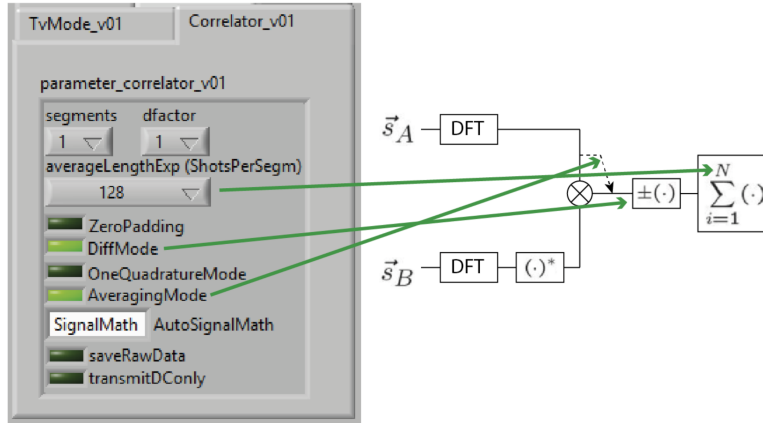Cleansweep. dfactor and ZeroPadding are used to control decimator.

Figure 4.11: Schematic of correlator and averager [12].

When DiffMode is on, the FPGA flips the sign of the product of s_A and s_B every other repetition, so that the summation in Averager is the sum of differences between two adjacent measurements. DiffMode is the key to measuring photo response by FPGA. When AveragingMode is on, s_B is discarded, and Averager calculates the average of N repetitions of s_A, instead of the summation. As we only have one input signal to FPGA, AveragingMode is always on during the study. If there is input to the ADC 2, it is possible to measure first order and second order correlation function. This is where the name of the application Correlator comes from [12] [19].

Effectively, we are measuring the difference of microwave power when turning the laser on and off as the AWG triggers the FPGA while being synchronized to laser intensity modulation and measuring microwave power at the FPGA. This leads to the interpretation of this signal as power eigenmode of the system as only those modes shift which are in the linear combination of normal mode. Formally one can think of this operation as a transformation from cavity modes to normal modes.

4.4.1 Photo Response Measurements

To map out the mode structure of our TBDT9-Array we have analyzed the photo response of the circuit. Subsequent measurements with laser turned on and laser turned off are taken by aligning the trigger of the FPGA with the modulation of the laser intensity. The differential mode implemented in the FPGA subtracts every other measurement taken by the FPGA and returns the photo response as a result. Advantages are the single measurement run that needs to be done and less influence of laser heating as claimed

by Chen [12]. Disadvantages are a noisy phase measurement in the regions with low amplitude, a lot of fitting parameters and a whole frequency sweep for every changed laser parameter. We have fitted the photo response with a composition of a Heaviside function and a gaussian (see App.) shown in Fig. 4.12a
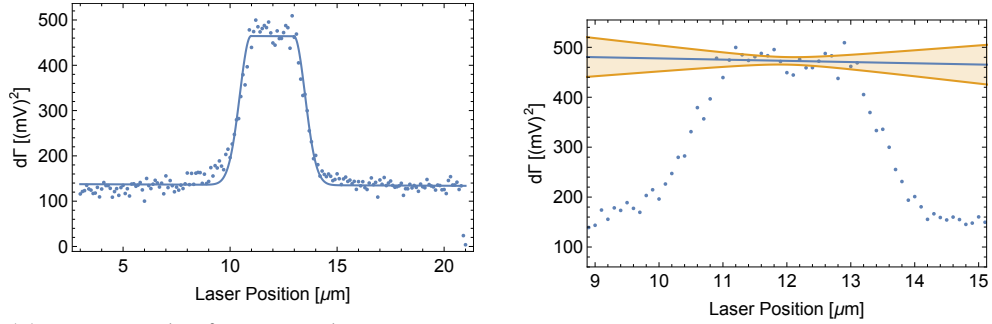
(a) An Example of a power photo response measurement where we have scanned the inductor line of resonator 3 (R3) at mode 2 with the laser.

(b) The 0.9 confidence band for a linear fit of data for photo response signal is on of the same mode as in (a).

Figure 4.12: Power Photo Response Measurement with FPGA in DiffMode.

For an upper bound of the error, we have calculated the standard error for a linear fit of the noise, when the laser is on the inductor line and generates high values for photo response signal. As we are only interested in in the amplitude of our signal, lower signal-to-noise ratio introduces higher amount of uncertainty to our signal with high values for $|d\Gamma|$ compared to the noise floor.

Chapter 5

Scientific Results

In this chapter, we present the results from laser scanning microscopy of our samples from mask 92. The mask consists of samples with seven and more resonators per array. In the first subsection, we discuss the dipstick measurements performed on the four recent approaches to new design paradigms. For the main part, we outline the concordance of our measurements of normal modes with theory and give insights for a next iteration of lumped-element resonator arrays.

5.1 Dipstick Measurements

We have measured the scattering matrix S_{ij} with the Agilent N5230 vector network analyzer (VNA) of multiple samples from Mask 92. The dipstick measurements where performed in liquid helium at a temperature of about 4.2 K which is below the critical temperature of 9.2 K where niobium is superconductive. We have calibrated the dipstick cables with a Rosenberger SMP Calibration Kit. The settings for the measurements shown in Fig. 5.1 were IF = 10 kHz, 50 calculated and measured averages and 10'000 points resolution. For a more detailed manual of the measurement process as sample assembly and calibration of the setup please read "Low Frequency Resonators on Superconducting Chips" by P. Lenggenhager and B. Mitchell [23] [14].

As discussed in Ch. 2 we expect nine chip modes - one for every resonator in the array. All design changes of the analyzed chips were attempts at gaining more symmetric behavior of the structures. We can visually inspect that the TBDT9-Array in Fig. 5.1 (d) is the ideal sample in this case as it behaves most similar to the theoretical prediction for perfectly symmetrical arrays.

(a) M92 BR9

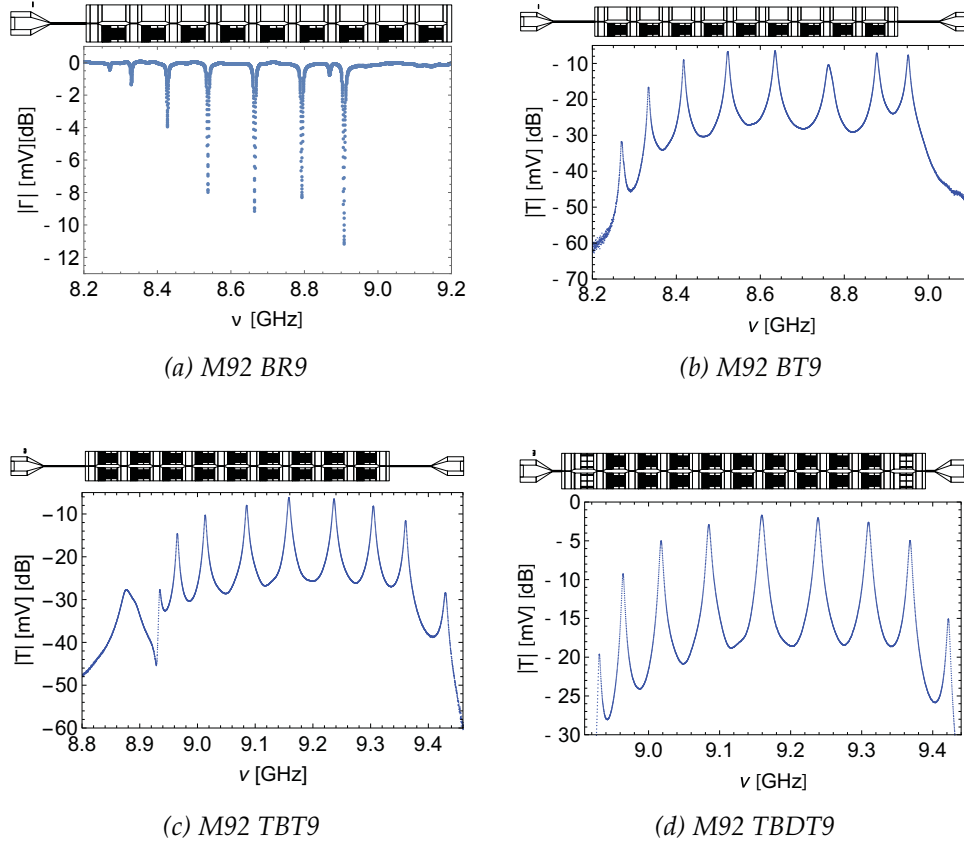*(b) M92 BT9*

(c) M92 TBT9

(d) M92 TBDT9

Figure 5.1: Reflection and Transmission coefficient of measured lumped-element resonator arrays on the M92 Mask (see Fig. A.1 in the Appendix). In (a) the reflection spectrum is shown as the structure is a reflection geometry.

An observation made with these measurements was that the transmission coefficient has much higher signal to noise ratio compared to the reflection coefficient. We concluded based on visual inspection of the coefficients shown in 5.1, without extraction of design parameters (e.g. by fitting these results), that the TBDT9-Array has the best undelaying design approach of the current mask. We can't expect fully symmetric behavior as there is still broken symmetry between the to coupling launchers. Based on these arguments we have chosen to further investigate the nature of symmetry breaking of the M92 TBDT9-sample by fitting the normal modes and eigenfrequencies and reconstruct the Hamiltonian of the chip.

5.2 Fitting Parameters and Symmetry Breaking

To extract the eigenvalues of the Hamiltonian of our system, a suitable approach is to measure and fit scattering parameters. In this thesis, we have fitted the reflection coefficient using Input-Output theory from Section 2.3.2 around every maximum as well as fitting the whole transmission coefficient.

Fitting of the TBDT9-Modes

In Sec. 5.4 we have characterized the TBDT9-Array using laser scanning microscopy using the eigenfrequencies shown in Tab. 5.1. The approach taken is explained in detail in Subsec. 5.2.

ν_1	ν_2	ν_3	ν_4	ν_5	ν_6	ν_7	ν_8	ν_9
8.966	9.000	9.055	9.123	9.199	9.280	9.355	9.414	9.443

Table 5.1: Eigenfrequencies ν_i (in GHz) for the Hamiltonian of the TBDT9-Array.
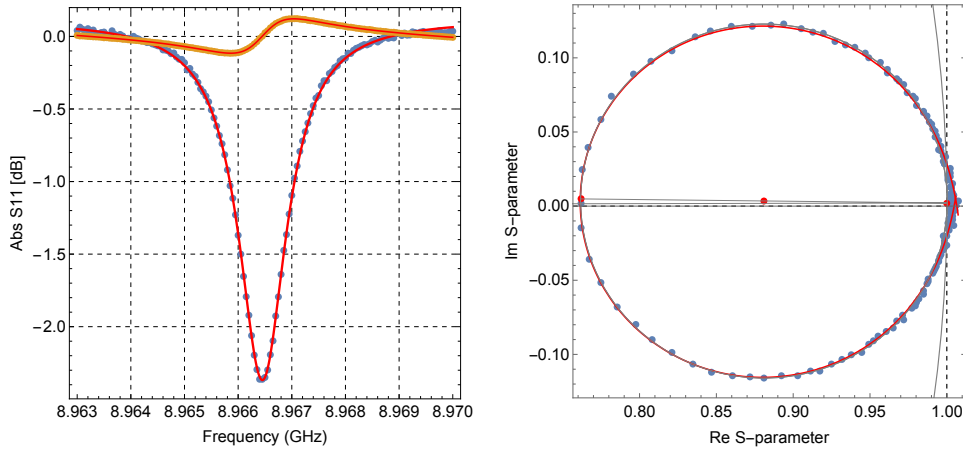
(a) Absolute value and phase of the reflection coefficient for the mode ν_1 as shown in Table 5.1.

(b) IQ-Plot in the complex plane of the reflection coefficient for the mode ν_1 as shown in Table 5.1.

Figure 5.2: An example of one of the nine fits performed on the reflection coefficient of the TBDT9-Array measured in the Arctic lab. Plots of phase and imaginary- and real part are in the Appendix.

Fitting Parameters

Since we measured not only single resonators but larger arrays of identical resonators, our first approach was to extract the parameters from a fit of

multiple individual local peak spectra. It turns out that the residual function does not have a unique local minimum in a neighborhood of consistent values of our simulations or design. This makes it impossible to find a unique set of S-parameters for the circuit. This observation makes numerical fitting a difficult problem. To avoid fitting the 36 parameters to our system we have made heuristic assumptions for our data:

We assume that our resonators couples stronger to the ground on the edges. Instead of having central elements strongly corrected, we choose to fix central elements of the coupling capacitances and allow larger variation for the edges. For the shunt capacitances we don't see any symmetry breaking and don't need to consider further adjustments of design parameters.

- Inductance was fixed to $L = 0.8595$ nH for all resonators.

- Inter-site coupling capacitance C_κ was perturbed on the edge to account for boundary effects like ground coupling or other parasitics. With every component of

$$C_{\kappa,i} = 9.523 \ (1 + \delta_i)_{1 \leq i \leq 10} \text{ fF} \tag{5.1}$$

is perturbed stronger for edge resonators with $0 \leq \delta_i \leq 1$ and $\delta_5 \simeq 0$.

- Resistance R was fixed to $R = 0.15 \ \Omega$ for all resonators.

- Shunt capacitance was set to $|C| = 329.6$ fF for every individual resonator where we perturbed every individual site by less than 1%.

$$C_i = 329.6 \ (1 + \delta_i)_{1 \leq i \leq 9} \text{ fF} \tag{5.2}$$

As explained earlier, we wanted to understand how the broken symmetry between the right and left launcher translates to S-parameters, Hamiltonian or normal modes. A plausible approach, explained in Sec. 5.3 is to fit the transmission coefficient of all modes and find the capacitances of the chip.

5.3 Characterization with Transmission Coefficient

With the theory developed in Ch. 2, we can experimentally attain the design parameters with Input-Output Theory and transfer matrix formalism. We have fitted the transmission coefficient which we measured in the Arctic Lab using the ansatz for the fitting parameters discussed in the previous Section. We were interested in the breaking of symmetry at the edges of coupling capacitances while holding the central elements fixed.

As depicted in Fig. 5.4, this approach gives us a correction of the right launcher coupling of approximately -25% for a possible next iteration of lumped-element resonators.
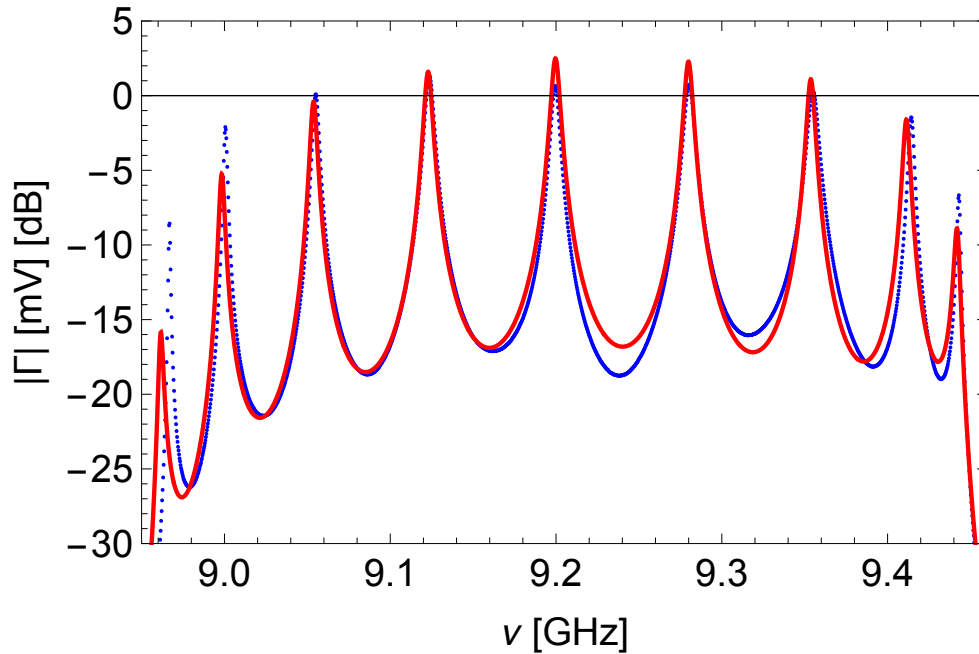

Figure 5.3: Transmission coefficient of TBDT9-Array as measured in the Arctic Lab. The measured data is depicted in blue and the fit using Input-Output formalism in red. For a depiction of the fitting parameters (see figure 5.4).

The δ_i-terms are negligible for all coupling capacities $C_{\kappa,i}$ except for $i = 2$ (second from left) which has a small perturbation from symmetric state of about +4% and the right launcher coupling with a large -25%. However, this result is not completely unambiguous. As mentioned, there is not a unique way of fitting the data, as the residual function does not have a unique mimimum.
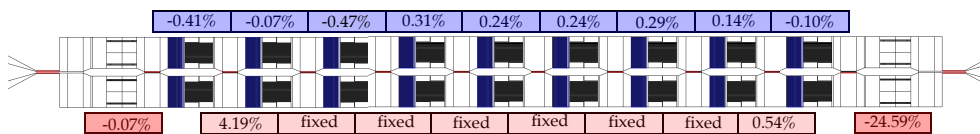
Figure 5.4: Illustration of perturbations δ_i from symmetric case of shunt capacitances C_i (blue) and coupling capacitances $C_{\kappa,i}$ (red) of fit in Fig. 5.3. See Eq. 5.2 and 5.2 for definition of these parameters.

To further investigate the behavior of the TBDT9-Array, we chose to analyze it with laser scanning microscopy. This method offers many more degrees of freedom to measure and characterize the array.

5.4 Characterization with Laser Scanning Microscopy

We have discussed in Sec. 2.3 how to write the Hamiltonian of the CRA dependent on inductive, capacitive and resistive parameters in detail. Solving for eigenvalues, which correspond in this case to the resonant frequencies, and for eigenvectors, in our case gives the normal modes.

The theoretical prediction for the Hamiltonian comes from the definitions of the matrix J and the vector ω in Eq. 2.3. In the construction of the Hamiltonian, we neglect non-nearest neighbor coupling terms, $J_{i,j} = 0$ with $i \leq i+2$ as they fall of quickly and are numerically not relevant for the eigenvalue problem. A thing to note is that we need to be careful which representation we choose, as in a non- symmetric case $C_{i,j} \neq C_{j,i}$ it does not hold that $\mathcal{H} = \mathcal{H}^T$. We have measured all physical resonators in the TBDT9-Array at all eigenfrequencies.

We have plotted mode structure with our sample with a fit using one residual function for all nine modes (as seen in Fig. 5.5).To avoid the problem of gauging the FPGA's power photo response measurements we have normalized $d\Gamma$ for both the measurement and fit. This approach is productive and sufficient for arriving at indications how to improve the iterations of chips. As we are measuring power, we have computed the square of every individual mode after solving the eigenvalue problem of the Hamiltonian for the fitting function.

In Fig. 5.5, we fit normalized modes squared and we are minimizing the Euclidean norm of every cavity mode of resonators R1 to R9. We can see that this plot resembles the mode structure of nine coupled pendulas. The biggest variation δ_i is at the right edge of the circuit (as seen in Fig. 5.6, which couples much stronger to the ground. We again, find a lower coupling capacitance C_κ for the right launcher of -15%. Like in the fit of transmission

coefficient data, there is a second perturbation which is not negligible. A possible explanation is that the residual converged to another minimum.
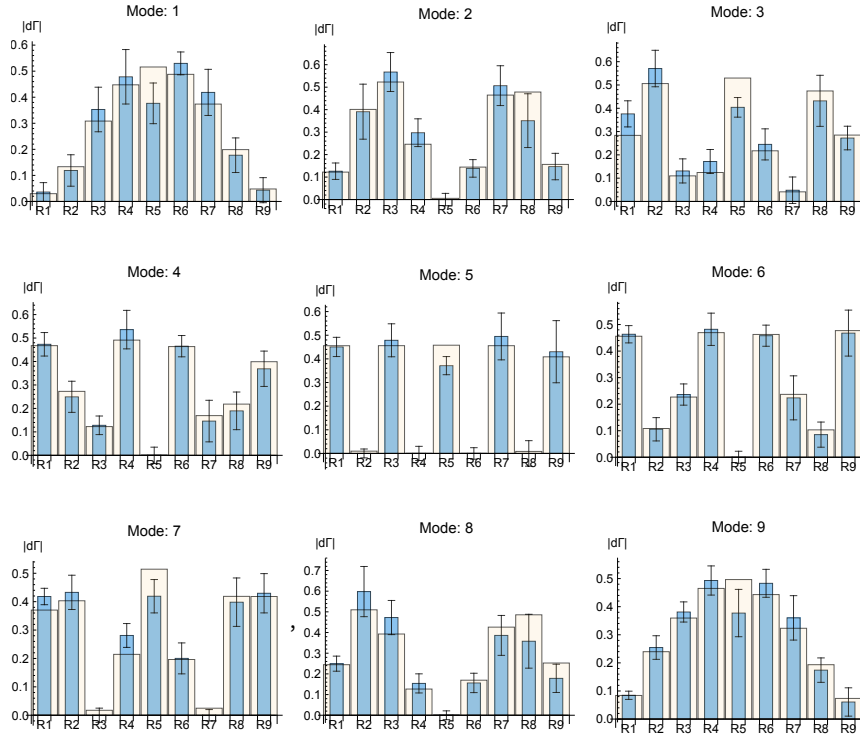

Figure 5.5: Photo response as a function of individual resonators. With bars depicted in blue we see power photo response for every mode (resonant frequency) at all nine resonators R1 to R9. The yellow bars show the fit of the data via construction of Hamiltonian. The eigenmodes of the measurement and the fit are normalized. Center coupling parameters where held fixed as shown in Table 5.6.
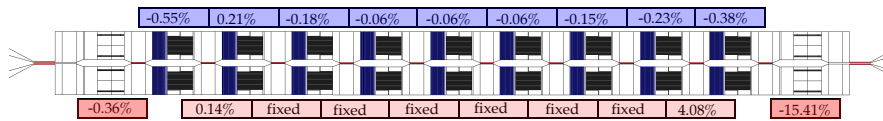

Figure 5.6: Illustration of perturbations δ_i from symmetric case of shunt capacitances C_i (blue) and coupling capacitances $C_{\kappa,i}$ (red) of fit in Fig. 5.5. See Eq. 5.2 and 5.2 for definition of these parameters.

Chapter 6

Discussion & Conclusion

In this thesis, we studied the mode structure and scattering matrix elements of arrays of lumped-element resonators. We have established theoretical predictions by analyzing the physics of the system, using the Lagrangian, Hamiltonian and Input-Output formalism. Further have we introduced the basic theory of photo response and laser scanning microscopy in Ch. 3.

In first assessment, we have identified using dipstick measurements which design approaches on the current M92 Mask work best. Afterwards, we have fitted the transmission coefficient on all modes using the Input-Output and transfer matrix formalism. To further improve understanding of the chip and the nature of symmetry breaking in the structure, we have used laser scanning microscopy. Laser scanning microscopy provides ways to probe and tune the properties of superconducting resonators. This technique will provide key insight into local properties of these photon lattices when interactions are strong, and an important tool for the study of nonequilibrium quantum phase transitions and quantum simulation [6].

The setup proved useful in analyzing the nature of symmetry breaking. We can conclude, that the symmetry is broken at the right launcher. Improvement is still required, as error estimates are just upper bound estimates in the current procedure. Furthermore, should the question be addressed, if we can gain complete insight into the mode structure of a lumped element resonator array by individually fitting the single Lorentzian. This would provide much easier scaling to avoid the numerical complexity of fitting scattering parameters of a many-site lattice.

In this thesis, we have demonstrated that laser scanning microscopy is a valuable tool for analyzing superconducting photonic quantum simulators. We have shown that the method works for non-trivial arrays. The next iteration should be arrays with increased coupling capacitances on the right launcher.

Appendix

All samples drawn on Wafer for the chip M92 can be seen. We have used Mathematica to draw this CAD-model. Please zoom in to get a good look at the Arrays.
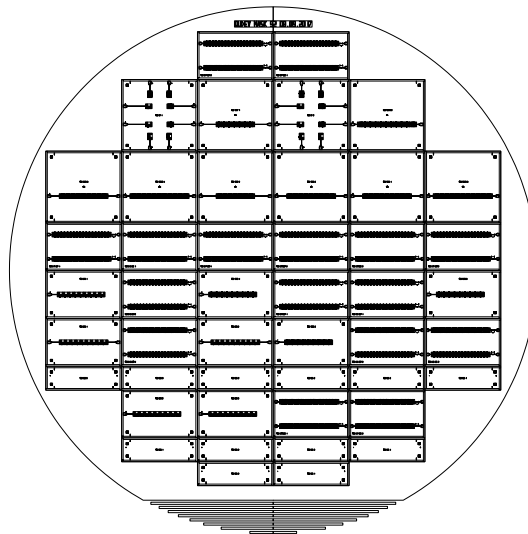

Figure A.1: Wafer for the M92 Chip series.

Photo Response Measurements

To fit the photo response as measured with FPGA, we have used the following function:

$$f(x) = \begin{cases} A + Bx + o, & |x - b| < \frac{w}{2} \\ Ae^{-\frac{\left(-b - \frac{w}{2} + x\right)^2}{2c^2}} + Bx + o, & x - b \geq \frac{w}{2} \\ Ae^{-\frac{\left(-b + \frac{w}{2} + x\right)^2}{2c^2}} + Bx + o, & x - b \leq \frac{w}{2} \end{cases}$$

Fitting and Plotting of Individual TBDT9-Modes

Often, the Q-factor and resonance frequency ν_0 are enough to characterize the measured resonator. However, it is necessary to fit the complex reflection coefficient obtained from Input-Output theory to extract the coupling and loss rates.
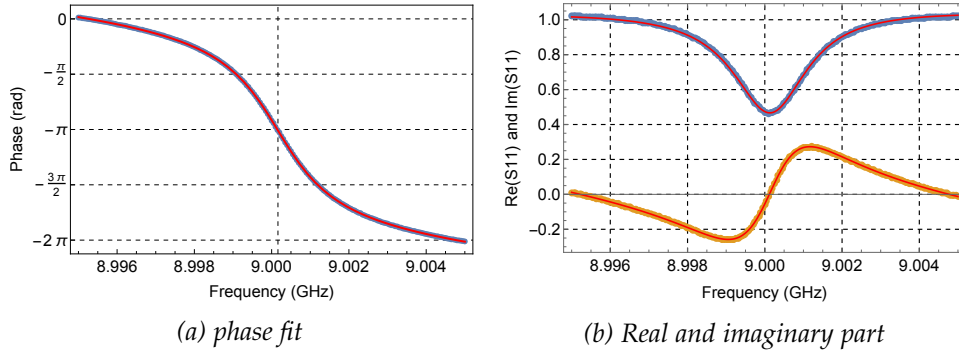

(a) phase fit *(b) Real and imaginary part*

Figure A.2: An example of one of the nine fits performed on the reflection coefficient of the TBDT9-Array measured in the Arctic lab.

In following Table, we have an experimental description of the TBDT9-Array using Input-Output formalism.

ν_0 (GHz)	κ (MHz)	γ (MHz)	ϕ	τ	$\Delta\phi$	Amplitude
8.966	0.156	1.106	127.162	-2.257	0.013	1.010
9.000	0.647	1.717	247.274	-4.373	0.046	1.026
9.054	1.516	2.498	63.604	-1.117	-0.031	0.998
9.123	2.608	2.959	155.659	-2.714	-0.056	1.038
9.199	2.685	2.758	253.169	-4.380	0.070	1.039
9.279	2.795	3.778	258.477	-4.430	-0.119	1.056
9.354	2.666	4.300	275.175	-4.682	0.056	1.065
9.414	1.688	1.935	305.559	-5.168	0.069	1.034
9.442	0.475	1.795	97.385	-1.642	0.024	1.008

Table A.1: All fitting parameters in Input-Output theory formalism for the TBDT9-Array on Mask 92. For fitting and generating plots mostly standard functions from the QUDEV library "LumpedElements4.m" where used.

Bibliography

[1] R. Feynman, "Quantum mechanical computers," *Foundations of Physics*, vol. 16, no. 6, pp. 507–531, 1986.

[2] M. Greiner, O. Mandel, T. Esslinger, T. W. Hansch, and I. Bloch, "Quantum phase transition from a superfluid to a Mott insulator in a gas of ultracold atoms," *Nature*, vol. 415, pp. 39–44, Jan. 2002.

[3] I. Bloch, J. Dalibard, and S. Nascimbène, "Quantum simulations with ultracold quantum gases," *Nat. Phys.*, vol. 8, pp. 267–276, 2012.

[4] R. Blatt and C. Roos, "Quantum simulations with trapped ions," *Nat. Phys.*, vol. 8, pp. 277–284, 2012.

[5] A. Aspuru-Guzik and P. Walther, "Photonic quantum simulators," *Nat. Phys.*, vol. 8, pp. 285–291, 2012.

[6] D. L. Underwood, W. E. Shanks, A. C. Y. Li, L. Ateshian, J. Koch, and A. A. Houck, "Imaging photon lattice states by scanning defect microscopy," *Phys. Rev. X*, vol. 6, p. 021044, Jun 2016.

[7] R. P. Budoyo, J. B. Hertzberg, C. J. Ballard, K. D. Voigt, Z. Kim, J. R. Anderson, C. J. Lobb, and F. C. Wellstood, "Effects of nonequilibrium quasiparticles in a thin-film superconducting microwave resonator under optical illumination," *Phys. Rev. B*, vol. 93, p. 024514, Jan 2016.

[8] A. Trabesinger, "Quantum simulation," *Nat. Phys.*, vol. 8, p. 263, 2012.

[9] A. Wallraff, D. I. Schuster, A. Blais, L. Frunzio, R.-S. Huang, J. Majer, S. Kumar, S. M. Girvin, and R. J. Schoelkopf, "Strong coupling of a single photon to a superconducting qubit using circuit quantum electrodynamics," *Nature*, vol. 431, pp. 162–167, 2004.

[10] A. Blais, R.-S. Huang, A. Wallraff, S. M. Girvin, and R. J. Schoelkopf, "Cavity quantum electrodynamics for superconducting electrical circuits: An architecture for quantum computation," *Phys. Rev. A*, vol. 69, pp. 062320–14, June 2004.

[11] R. J. Schoelkopf and S. M. Girvin, "Wiring up quantum systems," *Nature*, vol. 451, pp. 664–669, 2008.

[12] J. Chen, "Laser scanning microscopy of superconducting lumped element resonators," Master's thesis, ETH Zürich, 2015.

[13] D. M. Pozar, *Microwave engineering*. John Wiley & Sons, Inc., 4th ed. ed., 2011.

[14] A. Rubio Abadal, "Josephson parametric amplifiers with lumped-element coupled resonators," Master's thesis, ETH Zürich, 2015.

[15] D. F. Walls and G. J. Milburn, *Quantum Optics*. Berlin: Springer Verlag, 2 ed., 2008.

[16] O. B. Chun Tat Ngai, "Improved laser scanning microscopy method and characterization of annular lumped element resonators," Master's thesis, ETH Zurich, 2016.

[17] J. C. Culbertson and H. Newman, "Optical probe of microwave current distributions in high temperature superconducting transmission lines," *J. Appl. Phys.*, vol. 84, p. 5, 1998.

[18] G. F. Puebla-Hellmann, *DC, Microwave and Optical Measurement Schemes for Nano-Scale Devices*. PhD thesis, ETH Zurich, 01 2013.

[19] S. Gyger, "Improved measurement method for spatial-dependent photo response," Master's thesis, ETH Zurich, 2016.

[20] M. Peterer, "Investigating the suppression of external sources of decoherence in transmon qubits," Master's thesis, ETH Zurich, 06 2012.

[21] B. M. P. Lenggenhager, "Low frequency resonators on superconducting chips," Master's thesis, ETH Zurich, 2015.

[22] J. Chen and L. F. Wei, "Implementation speed of deterministic population passages compared to that of rabi pulses," *Phys. Rev. A*, vol. 91, p. 023405, Feb 2015.

[23] B. Mitchell and P. M. Lenggenhager, "Low frequency resonators on superconducting chips - a space-efficient lumped element design," semester thesis, ETH Zurich, 2015.

Acknowledgements

ETH

Eidgenössische Technische Hochschule Zürich
Swiss Federal Institute of Technology Zurich

Declaration of originality

The signed declaration of originality is a component of every semester paper, Bachelor's thesis, Master's thesis and any other degree paper undertaken during the course of studies, including the respective electronic versions.

Lecturers may also require a declaration of originality for other written papers compiled for their courses.

_____

I hereby confirm that I am the sole author of the written work here enclosed and that I have compiled it in my own words. Parts excepted are corrections of form and content by the supervisor.

Title of work (in block letters):

Authored by (in block letters):
For papers written by groups the names of all authors are required.

Name(s):   **First name(s):**

With my signature I confirm that
− I have committed none of the forms of plagiarism described in the '[Citation etiquette](#)' information sheet.
− I have documented all methods, data and processes truthfully.
− I have not manipulated any data.
− I have mentioned all persons who were significant facilitators of the work.

For papers written by groups the names of all authors are required. Their signatures collectively guarantee the entire content of the written paper.